

Stimulated Raman Scattering Microscopy with an All-Optical Modulator

Tobias Steinle,¹ Moritz Floess,¹ Andy Steinmann,^{1,*} Vikas Kumar,^{2,†} Giulio Cerullo,² and Harald Giessen¹

¹4th Physics Institute and Stuttgart Research Center of Photonic Engineering, University of Stuttgart, Pfaffenwaldring 57, 70569 Stuttgart, Germany

²IFN-CNR, Dipartimento di Fisica, Politecnico di Milano, Piazza Leonardo da Vinci 32, 20133 Milan, Italy

(Received 12 December 2018; revised manuscript received 14 February 2019; published 25 April 2019; corrected 2 May 2019)

Nonlinear phenomena are a frequent occurrence in nature and inherent to many optical systems. Nevertheless, nonlinearities are often avoided or suppressed in optical resonators. Here we demonstrate the application of nonlinear phenomena to pump-probe spectroscopy by using period doubling in a fiber-feedback optical parametric oscillator. On the basis of an analysis of the optical single-pulse spectra and successive second-harmonic spectra, we introduce a method to enhance the pulse-energy modulation depth to the level of conventional high-frequency modulators. We find that the modulator is suitable for high-speed, low-noise stimulated Raman scattering imaging with performance equal to that of acousto-optic modulation. The concept removes the need for electronic synchronization, reduces the detection effort and artifacts, and has great potential in terms of scalability of the modulation frequency.

DOI: 10.1103/PhysRevApplied.11.044081

I. INTRODUCTION

High-frequency optical modulation is a fundamental method with a variety of applications, including applications in optical metrology [1] and communications. It allows the separation of information-carrying signals from background noise, which often increases the signal-to-noise ratio by orders of magnitude. In the commonly used optical homodyne and heterodyne detection setups [2,3] probing is preferably performed at the Nyquist frequency (modulation at half the sampling frequency) to eliminate noise and favor short acquisition times [4,5]. Conventional electrically driven devices, such as acousto-optic modulators (AOMs) or electro-optic modulators (EOMs), are limited in modulation frequency and optical damage threshold, and require radio-frequency power electronics for driving. In the radio-frequency domain, the detection unit generally needs to be shielded to avoid cross talk with the driving electronics to minimize artifacts in the detected signal. For Nyquist detection, synchronous triggering of the modulator is required in addition. Optical modulation schemes based on graphene [6,7], semiconductor junctions [8], or plasmonics [9,10] have been demonstrated, but they are not suitable for high-power operation or are limited in modulation depth. Furthermore, they typically require an external synchronized control beam, which is clearly desirable for many applications, but is not helpful

for modulation spectroscopy, as it shifts the problem of generating the modulation to the control beam.

Here we present a technique that replaces electronic modulators with an all-optical approach, which achieves high modulation depth, is particularly suited for Nyquist detection, removes the need for synchronous triggering, and can potentially overcome the frequency-scaling limits of electronic modulators. The technique is based on period multiplication, which is a phenomenon of nonlinear dynamics that is frequently found in nonlinear optical systems. Prominent examples include fiber lasers and nonlinear ring resonators [11–17]. More generally, these (and other [18]) nonlinear systems exhibit chaotic attractors, limit cycles, and period- N attractors (“PN attractors”). A PN attractor corresponds to a state where an initial pulse in a resonator is reproduced every N th round trip. In this picture, the vast majority of mode-locked lasers operate in a P1 attractor, since every emitted pulse is identical. This case is called the “steady state.” The next case—namely, the P2 attractor—is also known as “period doubling.” It corresponds to a state where every second pulse that is emitted from a resonator is identical, leading to a period of the pulse train that is twice as long as the resonator round-trip time. This requires the pulse to alter periodically within two round trips, which requires a nonlinear element in the resonator. In synchronously pumped resonators, such as optical parametric oscillators (OPOs), period doubling generates a pulse train where every second pulse is attenuated, while an unmodulated reference beam can be obtained from the pump laser. This situation is ideally suited for modulation spectroscopy, since the maximum

*a.steinmann@pi4.uni-stuttgart.de

†Current address: University of Duisburg-Essen, Faculty of Chemistry, 45141 Essen, Germany.

possible modulation frequency is reached, the modulation is intrinsically synchronized, and no electronics are involved in the signal generation.

In this paper we characterize the nonlinear dynamics in a synchronously pumped fiber-feedback optical parametric oscillator (FFOPO) for the first time. The dispersive-Fourier-transformation (DFT) technique, which has been used, for example, for single-shot reconstruction of pulses in fiber ring cavities [19] or real-time measurement of spectral noise in supercontinuum generation [20], enables monitoring of the shot-to-shot dynamics of the FFOPO. We further introduce a method to enhance the modulation depth based on second-harmonic spectral compression [21,22] and particularly demonstrate its suitability for high-speed, low-noise stimulated Raman scattering (SRS) imaging.

II. ALL-OPTICAL MODULATOR

Our realization of the all-optical modulator is a fiber-feedback optical parametric oscillator [23–26], where the required nonlinearity in the feedback is provided by a single-mode optical fiber. As illustrated in Fig. 1, the pulse train of a mode-locked oscillator is used to pump the FFOPO. The pump laser is a home-built Yb:KGd(WO₄)₂ solid-state oscillator, which provides up to 8-W output power at 1032 nm with 450-fs pulse duration and a repetition rate of 41 MHz [27]. The resonator length of the FFOPO is chosen equal to the resonator length of the oscillator. The setup features four adjustable parameters. The parametric gain is controlled by the pump power and the phase-matching condition [28]. For this purpose, the MgO-doped periodically poled lithium niobate (PPLN) crystal is equipped with a heater and a set of poling periods. Further, the delay mismatch, which is the difference in the resonator length of the FFOPO and its pump oscillator, is adjustable. Lastly, the output coupling ratio is variable, which is used to balance the ratio of feedback nonlinearity and gain. For the later SRS experiment, the FFOPO signal beam is frequency doubled in another PPLN crystal.

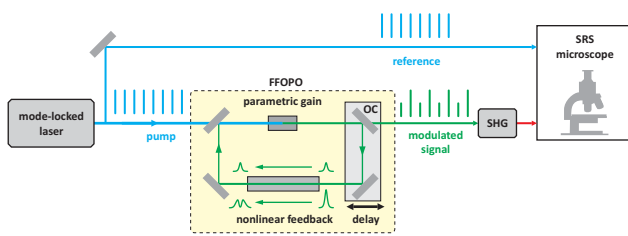


FIG. 1. The all-optical modulator is based on a fiber-feedback optical parametric oscillator with a nonlinear feedback medium and a second-harmonic generation stage (SHG). OC, variable output coupler.

We find that depending on the setting of the parameters, a rich variety of nonlinear dynamics can be observed (Fig. 2). A map of the parameter space is created by our sampling the FFOPO signal output with the oscilloscope using the DFT setup (details are given below). The cavity delay and pump power are increased in steps of 2 μm and 2 mW, which results in a dataset of 125 × 500 pulse trains of 80 individual pulses each. Processing is realized with a script that first extracts the pulse-energy sequence by averaging over 24.4-ns intervals (reciprocal of the repetition rate) and determines the state of operation (P1, P2, etc.) on the basis of a fast-Fourier-transform algorithm. This method is very reliable in distinguishing different PN attractors from one another and identifying chaotic regions, but it is prone to incorrectly classify limit cycles as close-by PN attractors. Hence, a second algorithm that compares the single-pulse spectra supports the analysis. Limit cycles are reliably identified, since in contrast to PN attractors they do not show repeating spectra after an integer number of round trips. Nevertheless, the identification is not always unambiguous, particularly for smooth, continuous transitions from limit cycles to PN cycles, such that a rather conservative tolerance setting is used that slightly favors P1, limit cycles, and chaos in the identification step.

For low intracavity pulse energy, either due to low pump power or high output coupling ratio, the FFOPO will generally operate in the steady state. An increase of intracavity pulse energy, however, triggers the nonlinearity to modify the feedback pulse via self-phase modulation. While Fig. 2(a) shows that this does not yet imply the occurrence of nonlinear phenomena, Figs. 2(b)–2(d) prove that for the correct choice of delay mismatch, the system undergoes transitions from the steady state into different PN attractors, limit cycles, and chaotic attractors. To show the relative location of these states with respect to each other, we map a piece of the parameter space by varying the delay mismatch and the pump power, as shown in Fig. 2(e) and, in projection, in Fig. 2(f). It is important to notice the dimensions of some of the attractors; for instance, the well pronounced P2 attractor that spans a pump power from 0.51 to 0.77 W in Fig. 2(b). It is further stable against delay variations of tens of micrometers, which, in combination, results in a very robust state of operation, enabling application as an all-optical modulator. The following experiments are performed with the system operating in a much-smaller stability region [indicated by the black circle at 775 mW and 156 μm in Fig. 2(f)], which is still perfectly sufficient for long-term investigations. This point shows rather high modulation depth, which at an absolute level of about 10% is still low compared with the requirements of a modulator. However, besides the pulse-energy modulation that is visualized in Fig. 2, the self-phase modulation also causes the spectral and temporal pulse shapes to oscillate, which is a unique feature of this type of modulator.

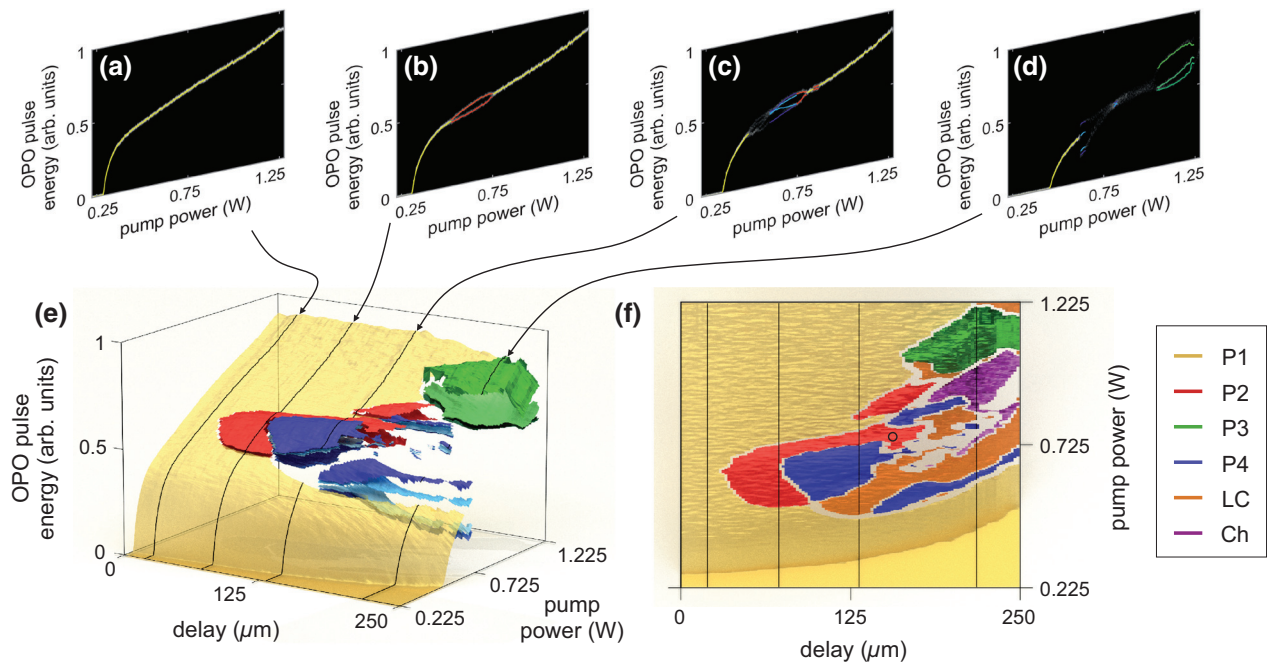


FIG. 2. Bifurcation diagrams of the FFOPO intracavity pulse energy for increasing cavity delay (a)–(d). The steady state (P1) is highlighted in yellow, P2 cycles are highlighted in red, P3 cycles are highlighted in green, and P4 cycles are highlighted in blue. The different hues of the colors are used to indicate the different branches of the PN cycles for better visibility. These measured cross sections can be combined to form a map of the parameter space (e). For clarity, limit cycles (LC) and chaos (Ch) are excluded. For this figure, the output coupling ratio and crystal temperature remain constant. The projection of (e) is shown in (f) and includes limit cycles (orange) and chaos (purple). The white regions are unstable or oscillating between different attractors. The black circle indicates a P2 cycle at a delay of $156\ \mu\text{m}$ and a power of $0.775\ \text{W}$, where later SRS measurements are performed (see Figs. 3–5).

To show that this spectral difference in the FFOPO signal pulses is useful to realize high modulation depth (more than 70%) if combined with narrowband frequency doubling, we record the single-pulse signal spectra at this point of operation. For this purpose, the DFT technique [29–31], as illustrated in Fig. 3(a), is used. A small portion of the emitted pulse train is therefore coupled into a 10-km-long SMF-28 fiber and stretched into the nanosecond domain, where electronic sampling is feasible. Detection is performed with a fiber-coupled reverse-biased $\text{In}_{1-x}\text{Ga}_x\text{As}$ diode and sampling is realized with a 4-GHz oscilloscope (DSO9404, Agilent). With $50\text{-}\Omega$ input impedance, the measurement bandwidth is limited to approximately 1.2 GHz, which corresponds to a spectral resolution of 4 nm. The temporal axis is converted into the spectral domain on the basis of the dispersion data from Corning. The absolute wavelength calibration is realized by our calculating the average of 80 single-pulse spectra and superimposing it on the simultaneously measured (time-averaged) spectrum from an optical spectrum analyzer.

Figure 3(c) reveals that the spectral difference is indeed significant. While the pulse with higher energy (“pulse 1,” black), is spectrally broad with a spectral dip at 1580 nm, the second pulse exhibits its highest spectral power density close to 1580 nm. A spectral filter could thus be used to

cut spectral portions from these pulses that result in pulse trains with significantly higher modulation depth. Here, in addition, we frequency double these pulses using second-harmonic spectral compression, which also acts as spectral filter. In our case the frequency-doubling crystal provides an acceptance bandwidth of approximately $11\ \text{cm}^{-1}$. We monitor the second-harmonic-generation (SHG) efficiency for each pulse individually while sweeping the SHG phase-matching condition and thus the SHG center wavelength by temperature tuning. Figure 3(d) shows that the wavelength-dependent SHG efficiency closely follows the single-pulse spectra, shown in Fig. 3(c). For this particular point of operation, the highest modulation depth is achieved at a SHG wavelength of 795 nm, where the doubling efficiency of pulse 2 is very low, while pulse 1 can still be efficiently frequency doubled. The SHG spectral compression is further advantageous as it cleans the optical spectrum [Fig. 3(d), blue] and pulse duration, which are both regulated by the phase-matching condition in the SHG crystal. Using this method, we obtain a modulation depth of approximately 80%, which is a value that is well acceptable for applications. It could be further optimized by dispersion control of the incident pulses, since second-harmonic spectral compression sensitively depends to the input pulse chirp [32].

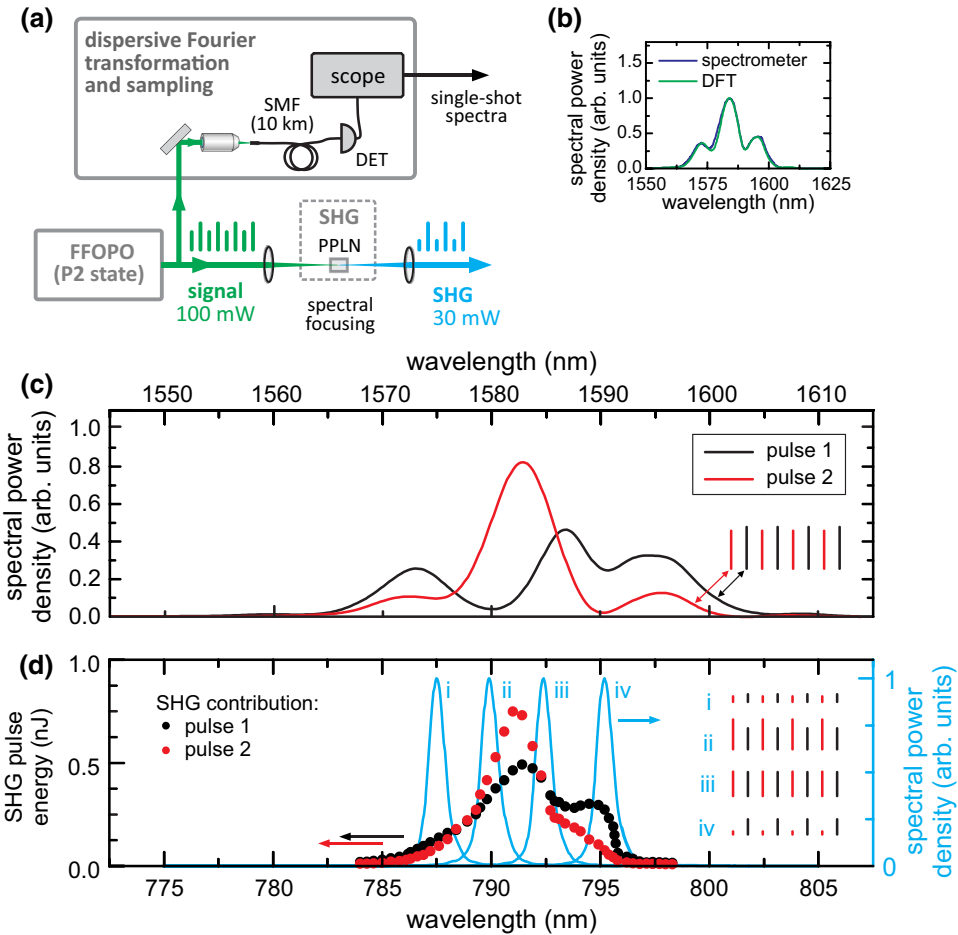


FIG. 3. (a) Setup for DFT and second-harmonic generation. (b) Combined spectrum as obtained by adding up the single-pulse spectra of two consecutive pulses (green) in comparison with a reference spectrum recorded with an optical spectrum analyzer (dark blue). (c) Single-pulse spectra of the two fundamental FFOPO pulses (black, red) prepared in a P2 attractor, as measured with the DFT oscilloscope. The inset showing the pulse train shows the actual energy ratio. (d) SHG pulse energy for the two different P2 pulses [colors according to the spectra in (c)] on variation of the SHG center wavelength by tuning the phase-matching wavelength of the SHG crystal. Exemplarily, four measured SHG spectra are shown in blue (i–iv) with an illustration of their corresponding pulse trains, indicating the experimental modulation depth at different SHG center wavelengths. DET, detector; SMF, single-mode fiber.

III. STIMULATED RAMAN SCATTERING MICROSCOPY

The capabilities of the all-optical modulator are shown in Fig. 4. We demonstrate that spectral tuning is possible [Fig. 4(a)] while maintaining a reasonable modulation depth between 70% and 80% [Fig. 4(b)]. We observe a deviation of the measured modulation depth depending on the actual position on the photodiode. In an AOM measurement the values could be compared with a power meter in the AOM *on* and *off* states, but this is not possible for the 20-MHz modulation here. We therefore give an approximate error of $\pm 5\%$ for the absolute value of the modulation depth. The spectral tuning is realized by operating the FFOPO in the identical P2 attractor while tuning its center wavelength. Within a limited spectral range this is feasible, since the nonlinear behavior, in particular the location

of the attractors in the parameter space, changes very smoothly. This is mainly because the overall intracavity group-delay dispersion and the phase-matching bandwidth change slowly with wavelength. While for many applications the tunability would be a minor aspect, it is extremely relevant in coherent Raman spectroscopy [2,33,34], which we demonstrate in the following with the example of a stimulated Raman scattering experiment. Moreover, the modulator is required to be stable over time, which we prove for our all-optical approach in Fig. 4(c). In a 60-min-long measurement at 790 nm, the modulation depth fluctuates by 0.5% rms. This value is not corrected for average power drift, which thus is already included in the fluctuations. During the wavelength sweep, the stimulated Raman gain (SRG) spectrum of acetone is recorded. The Raman pump pulses are obtained by frequency doubling the FFOPO output in a 10-mm-long PPLN crystal

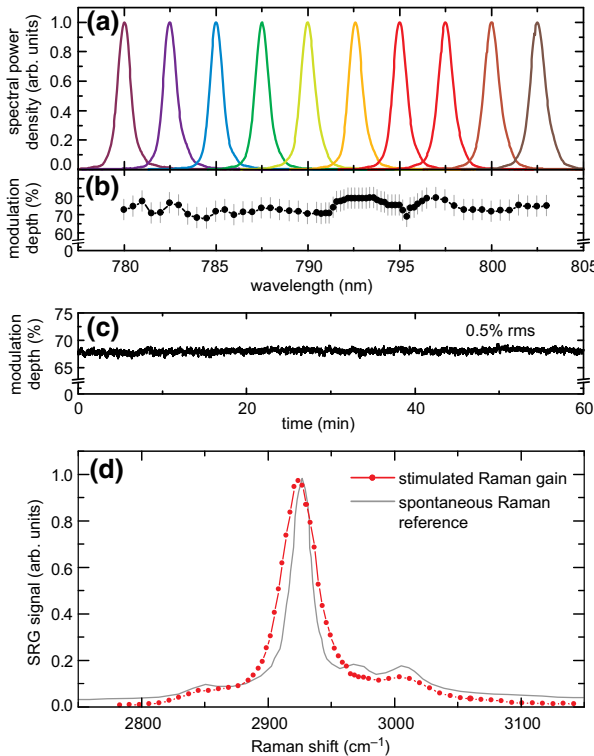


FIG. 4. (a) Spectra of the SHG in the P2 state. (b) Modulation depth versus wavelength obtained with a single P2 attractor. (c) Stability of the modulation depth over 1 h, sampled at a rate of 10 Hz. (d) SRG spectrum of acetone compared with the spontaneous Raman signal from the literature.

and using SHG spectral compression [21,22] to reduce the bandwidth to approximately 11 cm^{-1} , which corresponds to a pulse duration of approximately 1.5 ps.

The unmodulated 1032-nm Stokes pulses are obtained directly from the laser oscillator by spectral filtering with an etalon, resulting in pulses with bandwidth of approximately 8 cm^{-1} , which corresponds to a pulse duration of approximately 1.7 ps. An average pump power of 20 mW and an average Stokes power of 10 mW are used. Standard lock-in-based detection with a single-channel detector is used, as described, for instance, in Refs. [33,34]. The result is depicted in Fig. 4(d) and shows good quantitative agreement with the spontaneous Raman spectrum. We do not correct the values for the measured modulated power, since the measurement of the modulation depth is not sufficiently accurate. Figure 4(d) rather indicates that the true modulated power is more constant than our estimate from Fig. 4(b), since the only obvious discontinuity in the SRG signal occurs at 2965 cm^{-1} , where the poling period of the FFOPO crystal needs to be changed. The spectral resolution of the SRS measurement is determined by the bandwidths of the pump and Stokes pulses and thus by the etalon design and the length of the SHG crystal used for spectral compression. Accordingly, the performance of AOMs and P2-based modulators will be comparable.

We further compare the performance of the all-optical modulator based on the P2 attractor directly with an acousto-optic modulator that is inserted into the beam path after frequency doubling. When the AOM is used, the FFOPO is set to steady-state operation and the AOM is electronically synchronized to modulate the beam at half the repetition rate (20.5 MHz) of the oscillator. For this comparison, equal pulse energies of the higher-energy SHG pulse are used, while the lower-energy pulse depends on the modulation depth that the modulation mechanism produces. We find slightly higher modulation depth (80%)

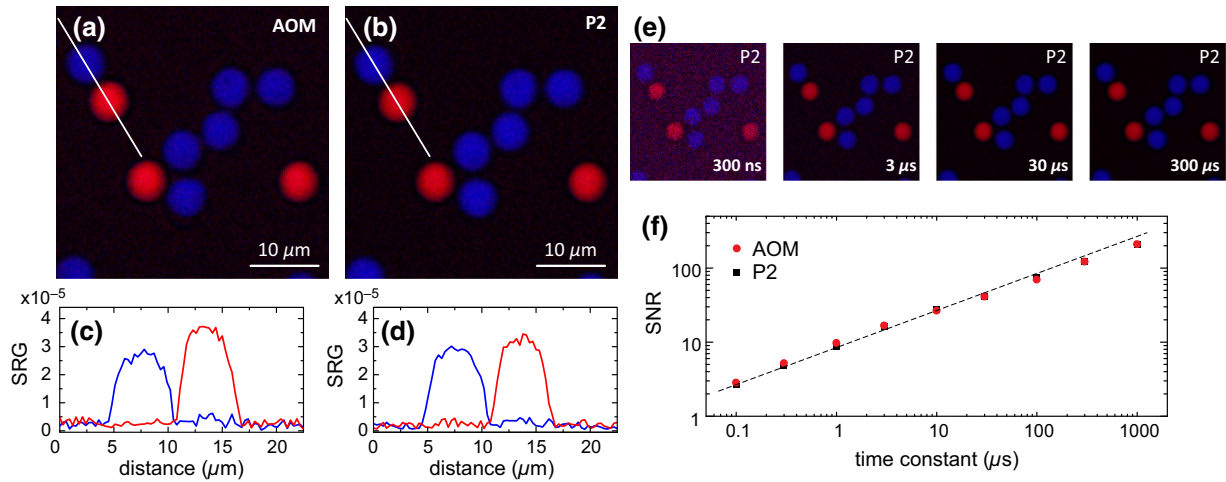


FIG. 5. Images (150 pixels by 150 pixels) of 6- μm PMMA and polystyrene beads in aqueous solution taken at Raman pump-Stokes frequency detunings of 2953 cm^{-1} (blue) and 3066 cm^{-1} (red) with a phase-locked AOM at $f_{\text{rep}}/2$ (a) and with the P2-based modulator (b), as well as corresponding cross sections (c),(d). The lock-in time constant is set to $10\text{ }\mu\text{s}$. The same image is shown for different time constants for the P2-based modulator (e). A comparison of the achieved signal-to-noise ratio (SNR) between the AOM (red) and the P2-based modulator (black) shows equal performance of both devices (f). All images are acquired with 10-mW pump power and 5.5-mW Stokes power on the sample.

for the AOM compared with the P2-based modulator (75%). With the P2-based modulator, in contrast, the noise floor of the lock-in amplifier is lower, due to the absence of electronic cross talk, which can amount to a relative signal offset of $(2 - 5) \times 10^{-7}$ in our setup. This value changes slightly due to environmental conditions, the quality of electrical shielding, and the difference in the detected phase between the SRS signal and the cross-talk signal. The magnitude is estimated by comparing the lock-in amplitude with the AOM enabled and disabled, both without the optical signal. A microscope with a galvanometric scanning unit is used to acquire images of a sample with polymer beads of $6\text{-}\mu\text{m}$ diameter in aqueous solution. Figure 5 shows the composite images of a scan at Raman pump-Stokes frequency detunings of 2953 cm^{-1} (blue) and 3066 cm^{-1} (red), when the conventional AOM is used [Fig. 5(a)] and when the P2-based modulator is used [Fig. 5(b)]. The quality of both images is well comparable, which is also evident in the analysis of the signal-to-noise ratio [Fig. 5(f)], where both modulators show equal performance. A sweep of the lock-in time constant [Fig. 5(e)] shows that even at 300 ns good image quality with clear chemical contrast is obtained, which would allow video-rate imaging of the 150-pixel-by-150-pixel section.

IV. CONCLUSION

In conclusion, we use the nonlinear dynamics in a fiber-feedback OPO to realize an all-optical modulator based on period doubling. A single device—namely, the fiber-feedback OPO—performs both frequency conversion and optical modulation. Second-harmonic spectral compression is used to enhance the modulation depth to 80%, while it simultaneously cleans up the spectral and temporal pulse shape. If frequency doubling is undesirable, similar results could be obtained at the fundamental frequency by use of a spectral pulse shaper. We further demonstrate that the performance of this modulator is equal to that of a conventional acousto-optic modulator in a stimulated Raman scattering microscopy experiment.

We believe that period-doubling modulation enables cutting-edge applications in the regime where conventional methods reach their limits. In the gigahertz range, AOMs cannot be used and EOMs are costly, sensitive to damage by optical power, and require bulky and powerful drivers. Besides its fundamental advantages of the intrinsic optical synchronization and low background noise due to the absence of electronic cross talk, period-doubling modulation is also interesting from a technical perspective: (i) since also the residual pump beam is modulated, it could be used as an optical in-line modulator for photonic integrated circuits; (ii) solely depending on the capabilities of the pump laser, it enables gigahertz modulation for frequency-comb spectroscopy at average powers that EOMs cannot

handle; (iii) it can boost the sensitivity of lab-on-a-chip sensing and spectroscopic applications at low cost and power consumption.

ACKNOWLEDGMENTS

We acknowledge support by the Carl Zeiss Foundation, ERC (ComplexPlas), BW-Stiftung, Deutsche Forschungsgemeinschaft, and BMBF.

- [1] A. Schliesser, N. Picqué, and T. W. Hänsch, Mid-infrared frequency combs, *Nature Photon.* **6**, 440 (2012).
- [2] E. O. Potma, C. L. Evans, and X. S. Xie, Heterodyne coherent anti-Stokes Raman scattering (CARS) imaging, *Opt. Lett.* **31**, 241 (2006).
- [3] B. Knoll and F. Keilmann, Scanning microscopy by mid-infrared near-field scattering, *Appl. Phys. A* **66**, 477 (1998).
- [4] Y. Ozeki, W. Umemura, Y. Otsuka, S. Satoh, H. Hashimoto, K. Sumimura, N. Nishizawa, K. Fukui, and K. Itoh, High-speed molecular spectral imaging of tissue with stimulated Raman scattering, *Nature Photon.* **6**, 845 (2012).
- [5] C. Riek, C. Kocher, P. Zirak, C. Kölbl, P. Fimpel, A. Leitnerstorfer, A. Zumbusch, and D. Brida, Stimulated Raman scattering microscopy by Nyquist modulation of a two-branch ultrafast fiber source, *Opt. Lett.* **41**, 3731 (2016).
- [6] W. Li, B. Chen, C. Meng, W. Fang, Y. Xiao, X. Li, Z. Hu, Y. Xu, L. Tong, H. Wang, W. Liu, J. Bao, and Y. R. Shen, Ultrafast all-optical graphene modulator, *Nano. Lett.* **14**, 955 (2014).
- [7] S. Yu, X. Wu, K. Chen, B. Chen, X. Guo, D. Dai, L. Tong, W. Liu, and Y. R. Shen, All-optical graphene modulator based on optical Kerr phase shift, *Optica* **3**, 541 (2016).
- [8] S. F. Preble, Q. Xu, B. S. Schmidt, and M. Lipson, Ultrafast all-optical modulation on a silicon chip, *Opt. Lett.* **30**, 2891 (2005).
- [9] D. Pacifici, H. J. Lezec, and H. A. Atwater, All-optical modulation by plasmonic excitation of CdSe quantum dots, *Nature Photon.* **3**, 55 (2007).
- [10] K. F. MacDonald, Z. L. Sámon, M. I. Stockman, and N. I. Zheludev, Ultrafast active plasmonics, *Nature Photon.* **3**, 55 (2009).
- [11] H. Nakatsuka, S. Asaka, H. Itoh, K. Ikeda, and M. Matsumura, Observation of Bifurcation to Chaos in an All-Optical Bistable System, *Phys. Rev. Lett.* **50**, 109 (1983).
- [12] G. Steinmeyer, D. Jaspert, and F. Mitschke, Observation of a period-doubling sequence in a nonlinear optical fiber ring cavity near zero dispersion, *Opt. Comm.* **104**, 379 (1994).
- [13] G. Sucha, S. R. Bolton, S. Weiss, and D. S. Chemla, Period doubling and quasi-periodicity in additive-pulse mode-locked lasers, *Opt. Lett.* **20**, 1794 (1995).
- [14] S. Coen, M. Haelterman, P. Emplit, L. Delage, L. M. Simohamed, and F. Reynaud, Experimental investigation of the dynamics of a stabilized nonlinear fiber ring resonator, *J. Opt. Soc. Am. B* **15**, 2283 (1998).
- [15] Q. Xing, L. Chai, W. Zhang, and C.-Y. Wang, Regular, period-doubling, quasi-periodic, and chaotic behavior in a self-mode-locked Ti:sapphire laser, *Opt. Comm.* **162**, 71 (1999).

- [16] J. M. Soto-Crespo, M. Grapinet, P. Grelu, and N. Akhmediev, Bifurcations and multiple-period soliton pulsations in a passively mode-locked fiber laser, *Phys. Rev. E* **70**, 066612 (2004).
- [17] P. Groß, N. Haarlammert, M. Kues, T. Walbaum, and C. Fallnich, Effects of optical feedback on femtosecond supercontinuum generation, *Opt. Fib. Tech.* **18**, 290 (2012).
- [18] R. M. May, Simple mathematical models with very complicated dynamics, *Nature* **261**, 459 (1976).
- [19] J. Hammer, P. Hosseini, C. R. Menyuk, P. St. J. Russell, and N. Y. Joly, Single-shot reconstruction of spectral amplitude and phase in a fiber ring cavity at a 80 MHz repetition rate, *Opt. Lett.* **41**, 4641 (2016).
- [20] B. Wetzel, A. Stefani, L. Larger, P. A. Lacourt, J. M. Merolla, T. Sylvestre, A. Kudlinski, A. Mussot, G. Genty, F. Dias, and J. M. Dudley, Real-time full bandwidth measurement of spectral noise in supercontinuum generation, *Sci. Rep.* **2**, 882 (2012).
- [21] M. Marangoni, D. Brida, M. Quintavalle, G. Cirmi, F. M. Pigozzo, C. Manzoni, F. Baronio, A. D. Capobianco, and G. Cerullo, Narrow-bandwidth picosecond pulses by spectral compression of femtosecond pulses in a second-order nonlinear crystal, *Opt. Express* **15**, 8884 (2007).
- [22] K. Moutzouris, F. Adler, F. Sotier, D. Träutlein, and A. Leitenstorfer, Multimilliwatt ultrashort pulses continuously tunable in the visible from a compact fiber source, *Opt. Lett.* **31**, 1148 (2006).
- [23] T. Südmeyer, J. Aus der Au, R. Paschotta, U. Keller, P. G. R. Smith, G. W. Ross, and D. C. Hanna, Femtosecond fiber-feedback optical parametric oscillator, *Opt. Lett.* **26**, 304 (2001).
- [24] K. A. Ingold, A. Marandi, M. J. F. Digonnet, and R. L. Byer, Fiber-feedback optical parametric oscillator for half-harmonic generation of sub-100-fs frequency combs around 2 μm , *Opt. Lett.* **40**, 4368 (2015).
- [25] F. Mörz, T. Steinle, A. Steinmann, and H. Giessen, Multi-Watt femtosecond optical parametric master oscillator power amplifier at 43 MHz, *Opt. Express* **23**, 23960 (2015).
- [26] T. Steinle, F. Mörz, A. Steinmann, and H. Giessen, Ultra-stable high average power femtosecond laser system tunable from 1.33 to 20 μm , *Opt. Lett.* **41**, 4863 (2016).
- [27] A. Steinmann, B. Metzger, R. Hegenbarth, and H. Giessen, in *CLEO: 2011 – Laser Science to Photonic Applications* (Optical Society of America, Baltimore, 2011) paper CThAA5.
- [28] G. Cerullo and S. De Silvestri, Ultrafast optical parametric amplifiers, *Rev. Sci. Instrum.* **74**, 1 (2003).
- [29] Y. C. Tong, L. Y. Chan, and H. K. Tsang, Fiber dispersion or pulse spectrum measurement using a sampling oscilloscope, *Electron. Lett.* **33**, 983 (1997).
- [30] D. R. Solli, G. Herink, B. Jalali, and C. Ropers, Fluctuations and correlations in modulation instability, *Nature Photon.* **6**, 463 (2012).
- [31] K. Goda and B. Jalali, Dispersive fourier transformation for fast continuous single-shot measurements, *Nature Photon.* **7**, 102 (2013).
- [32] M. Nejbauer, T. M. Kardaś, Y. Stepanenko, and C. Radzewicz, Spectral compression of femtosecond pulses using chirped volume Bragg gratings, *Opt. Lett.* **41**, 2394 (2016).
- [33] C. W. Freudiger, W. Min, B. G. Saar, S. Lu, G. R. Holtom, C. He, J. C. Tsai, J. X. Kang, and X. S. Xie, Label-free biomedical imaging with high sensitivity by stimulated Raman scattering microscopy, *Science* **322**, 1857 (2008).
- [34] T. Steinle, V. Kumar, M. Floess, A. Steinmann, M. Marangoni, C. Koch, C. Wege, G. Cerullo, and H. Giessen, Synchronization-free all-solid-state laser system for stimulated Raman scattering microscopy, *Light Sci. Appl.* **5**, e16149 (2016).

Correction: Figure 1 and its caption required modification, and they have been replaced.